

# Data-Driven Learnability Transition of Measurement-Induced Entanglement

Dongheng Qian<sup>1, 2</sup> and Jing Wang<sup>1, 2, 3, 4, \*</sup>

<sup>1</sup>*State Key Laboratory of Surface Physics and Department of Physics, Fudan University, Shanghai 200433, China*

<sup>2</sup>*Shanghai Research Center for Quantum Sciences, Shanghai 201315, China*

<sup>3</sup>*Institute for Nanoelectronic Devices and Quantum Computing, Fudan University, Shanghai 200433, China*

<sup>4</sup>*Hefei National Laboratory, Hefei 230088, China*

Measurement-induced entanglement (MIE) captures how local measurements generate long-range quantum correlations and drive dynamical phase transitions in many-body systems. Yet estimating MIE experimentally remains challenging: direct evaluation requires extensive post-selection over measurement outcomes, raising the question of whether MIE is accessible with only polynomial resources. We address this challenge by reframing MIE detection as a data-driven learning problem that assumes no prior knowledge of state preparation. Using measurement records alone, we train a neural network in a self-supervised manner to predict the uncertainty metric for MIE—the gap between upper and lower bounds of the average post-measurement bipartite entanglement. Applied to random circuits with one-dimensional all-to-all connectivity and two-dimensional nearest-neighbor coupling, our method reveals a learnability transition with increasing circuit depth: below a threshold, the uncertainty is small and decreases with polynomial measurement data and model parameters, while above it the uncertainty remains large despite increasing resources. We further verify this transition experimentally on current noisy quantum devices, demonstrating its robustness to realistic noise. These results highlight the power of data-driven approaches for learning MIE and delineate the practical limits of its classical learnability.

Quantum entanglement is a central resource of quantum information science, enabling advantages in computation, communication, and sensing [1–5]. Importantly, entanglement need not arise solely from coherent unitary evolution: suitably chosen and adaptively processed measurements can also generate nonlocal correlations in many-body systems [6–9]. This measurement-induced entanglement (MIE) underlies measurement-based quantum computation [10], enables rapid preparation of long-range entangled states [11–15], and gives rise to novel non-equilibrium phases of matter [16–20]. In particular, in hybrid unitary–measurement dynamics, competition between scrambling and projective measurements produces a measurement-induced phase transition (MIPT), across which the scaling of MIE changes from volume law to area law [21–37].

Despite its conceptual and practical significance, directly characterizing MIE in experiments remains notoriously challenging [38]. The central obstacle is post-selection: probing properties of a state conditioned on a specific measurement outcome requires repeating the experiment until that outcome reoccurs, an effort that grows exponentially with the number of measurements by Born’s rule. Several scalable diagnostics have been proposed to circumvent this bottleneck, including purification of an entangled reference qubit [39–43], learnability of conserved quantities [44] or of the pre-measurement state [45], cross-entropy benchmarks [46–48] and other machine-learning proxies [49–51]. Although these proxies successfully reflect the distinct behavior of MIE in different regimes and help reveal its critical behavior, they remain indirect witnesses rather than quantitative estimators of MIE itself. Recent works have made progress showing promise and limits [52, 53]. On the one hand,

MIE can in principle be estimated without post-selection by leveraging quantum-classical correlations, but this requires priori knowledge of the underlying quantum dynamics and the accuracy of estimation hinges on the fidelity of classical simulations. On the other hand, Ref. [53] proves that, without any knowledge of the pre-measurement state, no learning protocol can extract properties beyond ensemble averages using only a polynomial number of measurement shots. The practical limits of experimentally detectable MIE thus remain an open question.

Motivated by the recent success of data-driven quantum learning methods based solely on measurement records [54–56], we ask in this Letter: under what conditions can MIE be learned with polynomial resources from data alone—i.e., without post-selection and without any prior knowledge of state preparation? To address this question, we study the entanglement generated between two distant qubits  $A$  and  $B$  after all other qubits in a many-body state are measured. Using measurement outcomes only, we train a transformer-based neural network in a self-supervised manner to estimate the post-measurement state on  $AB = A \cup B$  conditioned on a given measurement outcome. Instead of reconstructing MIE directly, we estimate the total entanglement entropy of  $AB$ , which we use as an uncertainty metric quantifying the learnability of MIE. We focus on two settings—random one-dimensional (1D) all-to-all circuits and two-dimensional (2D) nearest-neighbor circuits—and in both we observe a clear learnability transition with increasing circuit depth. In the learnable phase, the uncertainty decreases with additional measurement data and model parameters, reflecting increasing time and space complexity. In the unlearnable

phase, the uncertainty saturates or even grows. We further probe this learnability transition in the presence of noise through simulations and experiments on IBM QPU `ibm_marrakesh`, finding that the transition remains observable under realistic noise. Overall, our results demonstrate the power of data-driven methods to extract informative features of the post-measurement state that reveal MIE, while simultaneously clarifying the fundamental limitations of learning MIE from measurement data alone. We note that a recent study [57] investigated MIE learnability for GHZ and cluster states using a similar data-driven approach, where signatures of a learnability transition were observed for the latter upon tuning the measurement direction. In contrast, our work addresses generic states generated by random quantum circuits and provides an explicit characterization of the emergence of distinct learnable and unlearnable regimes.

*Quantifying learnability*—We quantify the learnability of MIE as follows. Consider an  $L$ -qubit pure state  $|\psi\rangle$ . All qubits except two distant ones,  $A$  and  $B$ , are measured in the computational basis, yielding outcome  $m$ . The corresponding post-measurement state on  $AB$  is  $\sigma_{AB,m}$ , with reduced state  $\sigma_{A,m} = \text{Tr}_B(\sigma_{AB,m})$ . The MIE between  $A$  and  $B$  is defined as the average entanglement entropy  $\mathbb{E}_m[S_{A,m}]$ ,  $S_{A,m} = -\text{Tr}(\sigma_{A,m} \log \sigma_{A,m})$ , where  $\mathbb{E}_m$  denotes averaging over all measurement outcomes. Although evaluating  $\mathbb{E}_m[S_{A,m}]$  exactly is difficult due to post-selection, two-sided bounds can be given once a classical estimator  $\rho_{AB,m}$  of  $\sigma_{AB,m}$  is provided [52]. Nonnegativity of the relative entropy  $D(\sigma_{A,m} \parallel \rho_{A,m}) \equiv \text{Tr}[\sigma_{A,m}(\log \sigma_{A,m} - \log \rho_{A,m})] \geq 0$  implies the upper bound  $S_{A,m} \leq S_{A,m}^{\text{QC}}$ , where  $S_{A,m}^{\text{QC}} \equiv -\text{Tr}(\sigma_{A,m} \log \rho_{A,m})$  is the quantum-classical entropy. Monotonicity under partial trace,  $D(\sigma_{AB,m} \parallel \rho_{AB,m}) \geq D(\sigma_{A,m} \parallel \rho_{A,m})$ , then yields:

$$S_{A,m}^{\text{QC}} \geq S_{A,m} \geq S_{A,m}^{\text{QC}} - S_{AB,m}^{\text{QC}}, \quad (1)$$

which utilizes  $S_{AB,m} \geq 0$ . Thus, the true entanglement  $S_{A,m}$  lies within an interval of width  $S_{AB,m}^{\text{QC}}$  for each outcome  $m$ . Nevertheless, directly computing  $S_{AB,m}^{\text{QC}}$  requires complete knowledge of  $\sigma_{AB,m}$ . To access this quantity, we employ classical shadow tomography [58]. Qubits  $A$  and  $B$  are measured in random single-qubit Pauli basis, producing classical snapshots  $\sigma_{AB,m}^s$  that are an unbiased estimators satisfying  $\mathbb{E}_s[\sigma_{AB,m}^s] = \sigma_{AB,m}$ , where  $\mathbb{E}_s$  denotes averaging over different snapshots. We then define

$$\Delta \equiv \mathbb{E}_m \mathbb{E}_s [S_{AB,m}^{\text{SC}}] = \mathbb{E}_m [S_{AB,m}^{\text{QC}}], \quad (2)$$

where  $S_{AB,m}^{\text{SC}} \equiv -\text{Tr}(\sigma_{AB,m}^s \log \rho_{AB,m})$  is the shadow-classical entropy. Random single-qubit Pauli rotations on  $A$  and  $B$ , followed by computational-basis measurements of all qubits, jointly implement the averaging over both  $m$  and classical snapshots, consolidating the

two expectations and making  $\Delta$  experimentally accessible. Since  $S_{AB,m}^{\text{QC}}$  bounds the width of the interval containing the true entanglement, the quantity  $\Delta$  directly tracks the uncertainty of MIE and therefore quantifies its learnability. Importantly,  $\Delta$  depends on both the estimator and the true post-measurement state  $AB$ , and satisfies  $\Delta \geq \mathbb{E}_m[S_{AB,m}]$  with equality if and only if  $\rho_{AB,m} = \sigma_{AB,m}$  for all  $m$ . For a pure  $|\psi\rangle$ , one has  $\mathbb{E}_m[S_{AB,m}] = 0$ , so a perfect estimator achieves zero uncertainty.

*Machine-learning model*—Rather than estimating  $\rho_{AB,m}$  by classically simulating the state-preparation dynamics, we learn it directly from the measurement data. We parameterize  $\rho_{AB,m}$  with a neural network and train it to approximate the true post-measurement state  $\sigma_{AB,m}$ . To construct the loss function, we use the inequality  $\mathbb{E}_m[\text{Tr}(\sigma_{AB,m} - \rho_{AB,m})^2] \geq 0$ , which implies

$$\begin{aligned} & \mathbb{E}_m \mathbb{E}_s [2\text{Tr}(\rho_{AB,m} \sigma_{AB,m}^s) - \text{Tr}(\rho_{AB,m}^2)] \\ & \leq \mathbb{E}_m [\text{Tr} \sigma_{AB,m}^2] \leq 1. \end{aligned} \quad (3)$$

The first equality saturates if and only if  $\rho_{AB,m} = \sigma_{AB,m}$  for all  $m$ , and the second becomes an equality when  $\sigma_{AB,m}$  is pure. This motivates the loss function:

$$\mathcal{L}(\theta) = -\mathbb{E}_m \mathbb{E}_s [2\text{Tr}(\rho_{AB,m} \sigma_{AB,m}^s) - \text{Tr}(\rho_{AB,m}^2)], \quad (4)$$

where  $\theta$  denotes the model parameters. We adopt this loss rather than directly targeting  $\Delta$  because  $\text{Tr}(\rho_{AB,m} \sigma_{AB,m}^s)$  is bounded, while  $S_{AB,m}^{\text{SC}}$  exhibits unbounded fluctuations [52]. Alternative loss functions were also examined; detailed comparisons are provided in the Supplemental Material [59]. Importantly, this approach uses only experimentally accessible data: the labels  $\sigma_{AB,m}^s$  are directly reconstructed from measurements on  $A$  and  $B$ , enabling fully self-supervised training.

For the model architecture, we employ a transformer-based encoder consisting of multi-head self-attention layers and feed-forward blocks [60, 61]. Transformers efficiently capture long-range correlations, making them well-suited for modeling the nonlocal dependence of  $\rho_{AB,m}$  on global measurement patterns. Each measurement outcome  $m$ , represented as a binary sequence of  $\{+1, -1\}$ , is augmented with a [CLS] token at the beginning and encoded into high-dimensional representations. A specialized density matrix head then maps the [CLS] token's hidden state to a  $4 \times 4$  complex-valued density matrix, with hermiticity, positive semi-definiteness, and unit trace constraints automatically satisfied by construction. A schematic workflow is shown in Fig. 1(a), with architectural details provided in [59]. For a fixed quantum state, the training set contains  $N_m$  measurement shots, which defines the quantum time complexity, while the model contains  $N_p$  trainable parameters, reflecting the classical space complexity. Practical classical learnability without post-selection is feasible only if  $N_m$  and  $N_p$  do not grow exponentially with  $L$ . After training, we

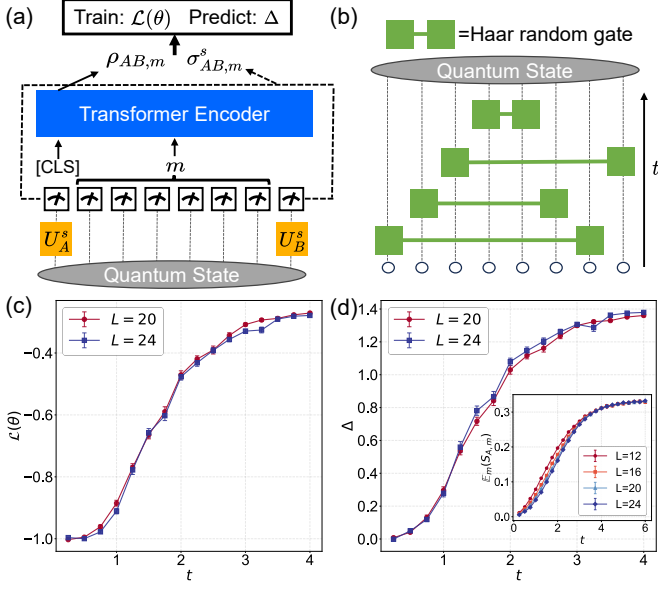


FIG. 1. Setup and learnability transition. (a) Schematic workflow. Given a quantum state, random single-qubit rotations  $U_A^s$  and  $U_B^s$  are applied to qubits  $A$  and  $B$ , after which all qubits are measured projectively in the computational basis. Measurement outcomes on all qubits except  $A$  and  $B$  are fed into a transformer encoder that outputs  $\rho_{AB,m}$ , while the outcomes on  $A$  and  $B$  are used to construct the classical snapshot  $\sigma_{AB,m}^s$ . The loss  $\mathcal{L}(\theta)$  and uncertainty  $\Delta$  are computed from these quantities. Notably, no prior knowledge of the state-preparation procedure is required. (b) Structure of the 1D random all-to-all circuit. (c)  $\mathcal{L}(\theta)$  as a function of circuit depth  $t$  for different system size  $L$ . Error bars denote the standard error over  $M = 50$  different circuit realizations. (d)  $\Delta$  as a function of  $t$  for different  $L$ . The inset shows the MIE between  $A$  and  $B$ . Each point is averaged over  $5 \times 10^4$  circuit realizations; the associated standard error is smaller than the symbol size.

evaluate the learned estimator using an independent set of  $N_e$  shots to compute  $\Delta$  via Eq. (2).

*Learnability transitions*—We first consider states generated by a 1D random all-to-all circuit, as illustrated in Fig. 1(b). At each discrete time step  $\delta t$ , we apply  $L\delta t$  Haar-random two-qubit gates between uniformly chosen pairs of qubits. For each depth  $t$ , we average over  $M = 50$  independently sampled circuit instances to capture average-case behavior. All training data are obtained from exact classical simulations of the circuit dynamics. We first train on a system of size  $L = 20$  using  $N_p = 7 \times 10^4$  model parameters and  $N_m = 8 \times 10^4$  measurement shots, both well within the polynomial-resource regime  $N_p, N_m \ll 2^L$  for learning process. Additional hyperparameters are provided in [59]. Fig. 1(c) shows that the training loss  $\mathcal{L}(\theta)$  converges to its lower bound  $-1$  for shallow depths. As  $t$  increases, the loss rises, indicating that the learned estimator  $\rho_{AB,m}$  fails to reproduce the true post-measurement state. To quantify MIE uncer-

tainty, we evaluate  $\Delta$  using  $N_e = 5 \times 10^4$  independent samples. As shown in Fig. 1(d),  $\Delta$  increases with  $t$  and saturates near  $2 \log(2)$ . This saturation suggests that at large  $t$ , the model outputs a maximally mixed state regardless of the measurement outcomes. Alternative loss functions may encourage pure-state predictions, but at large  $t$  the predicted state becomes nearly orthogonal to the true one, still producing large  $\Delta$  [59].

This learnability transition directly reflects an intrinsic computational phase transition in random quantum circuits, closely related to a finite-depth many-body teleportation transition [62]. As shown in the inset of Fig. 1(d), the MIE between  $A$  and  $B$  exhibits a finite-depth transition. Below a critical depth, the dynamics remain in a non-teleporting regime, correlations are essentially local, MIE vanishes as the system size becomes larger, and efficient classical algorithms exist for approximate random-circuit sampling and the dynamics exhibit low effective complexity [63]. In this regime, states are expected to admit efficient learning [64], implying that suitably designed neural networks can achieve accurate estimation with polynomial data and parameters resources [65]—the learnable phase. Beyond the critical depth, the circuit enters a teleporting regime where long-range entanglement emerges. Efficient classical simulation is believed to fail here, rendering average-case random-circuit sampling computationally intractable and establishing the basis of quantum computational advantage [66]. Therefore, polynomial-resource machine-learning models are not expected to succeed—defining the unlearnable phase. From this perspective, the learnability transition provides a direct machine-learning probe of computational complexity, faithfully tracking the underlying computational phase boundary. To demonstrate the finite-depth nature of this transition, we compare the results across different system sizes  $L = 24$  using the same  $N_p$  and  $N_m$ . At small  $t$ ,  $\Delta$  for  $L = 24$  is comparable to or smaller than that for  $L = 20$ . As  $t$  increases, the curves cross, indicating that the transition occurs at a finite depth. Accurately determining the critical depth would require simulations at larger  $L$  to minimize finite-size effects.

To further characterize the two phases, we fix  $L = 20$  and vary  $N_p$  and  $N_m$ . Detailed model architectures corresponding to different  $N_p$  are provided in [59]. Throughout we ensure  $N_p, N_m \ll 2^L$ . Fixing  $N_p = 7 \times 10^4$  and varying  $N_m$ , Fig. 2(a) shows that at small  $t$ ,  $\Delta$  decreases as data  $N_m$  increases, indicating that additional samples improve the model’s ability to extract MIE. In contrast,  $\Delta$  saturates at large  $t$ , suggesting the presence of an unlearnable phase where the polynomial of many samples does not lead to significant improvement. Fixing  $N_m = 5 \times 10^4$  and varying  $N_p$ , Fig. 2(b) shows that increasing  $N_p$  improves performance at small  $t$ , while  $\Delta$  saturates or even grows at large  $t$ . For excessively large  $N_p$ ,  $\Delta$  increases for all depths due to overfitting from insufficient training data. The combined dependence on  $N_p$  and

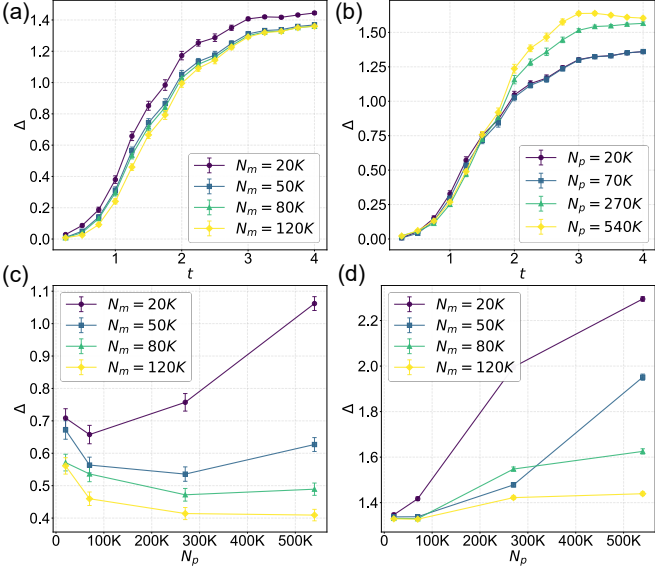


FIG. 2. Learnability transition in 1D random all-to-all circuits for  $L = 20$ . (a)  $\Delta$  versus depth  $t$  for varying  $N_m$  with  $N_p = 7 \times 10^4$  fixed. (b)  $\Delta$  versus depth  $t$  for varying  $N_p$  with  $N_m = 8 \times 10^4$  fixed. (c,d)  $\Delta$  as a function of  $N_m$  and  $N_p$  for representative depths  $t = 1.25$  and  $t = 3.5$ , respectively.

$N_m$  is shown in Fig. 2(c) and Fig. 2(d) for  $\Delta(t = 1.25)$  and  $\Delta(t = 3.5)$ , respectively. At  $t = 1.25$ ,  $\Delta$  clearly decreases with both resources (except in the strongly overparameterized regime where overfitting causes  $\Delta$  to grow). By contrast, at  $t = 3.5$ ,  $\Delta$  rapidly saturates and even grows despite the same increase in  $N_p$  and  $N_m$ , thus sharply distinguishing the learnable and unlearnable phases.

We next examine 2D circuit with nearest-neighbor couplings. We consider a square lattice with periodic boundary conditions, where at each step  $L\delta t$  two-qubit gates act only on adjacent qubit pairs. This setup is also known to exhibit a finite-depth computational transition [63, 67–70]. For a system of size  $L = 5 \times 5$ , varying  $N_p$  and  $N_m$  as in the 1D case, we observe the same qualitative behavior: for small  $t$ ,  $\Delta$  decreases markedly as either resource increases, indicating a learnable phase in which additional data or model capacity improves the MIE estimate; while at large  $t$ ,  $\Delta$  saturates or grows with increasing resources, signaling the unlearnable phase, as shown in Fig. 3(a,b). The dependence of  $\Delta(t = 1.6)$  and  $\Delta(t = 6.4)$  on different combinations of  $N_p$  and  $N_m$  [Fig. 3(c,d)] mirrors the 1D case, reinforcing the presence of distinct learnable and unlearnable phases.

*Noisy device*—The preceding analysis assumes ideal, noiseless circuit dynamics. However, in realistic experiments, noise introduces two key effects. First, each nominally identical state-preparation run experiences a different and unknown noise realization, making it harder for the model to extract consistent information from

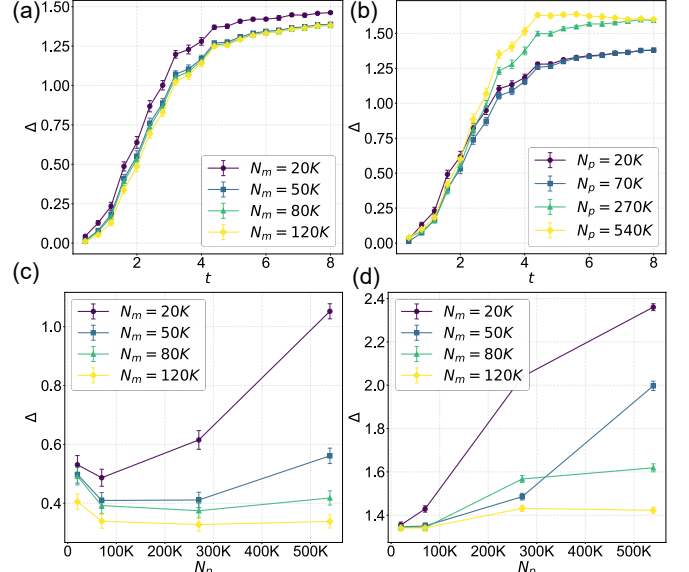


FIG. 3. Learnability transition in 2D nearest-neighbor circuits for  $L = 5 \times 5$ . (a)  $\Delta$  versus  $t$  for varying  $N_m$  with  $N_p = 7 \times 10^4$  fixed. (b)  $\Delta$  versus  $t$  for varying  $N_p$  with  $N_m = 8 \times 10^4$  fixed. (c,d)  $\Delta$  as a function of  $N_m$  and  $N_p$  at representative depths  $t = 1.6$  and  $t = 6.4$ , respectively.

measurement records. Second, noise renders the post-measurement state  $\sigma_{AB,m}$  mixed rather than pure, leading to  $\mathbb{E}_m[S_{AB,m}] > 0$ . As discussed above, this finite entropy constitutes an intrinsic contribution to the uncertainty of MIE and cannot be eliminated by improving model accuracy. To examine these effects, we combine noisy numerical simulations with direct experiments on current superconducting quantum processors. As a first step, we adopt a noise model based on the Qiskit snapshot of the IBM QPU ibm\_brisbane backend. For a 1D all-to-all circuit with  $L = 16$ , Fig. 4(a,b) show that the learnability transition remains visible, although  $\Delta$  is systematically larger than that in the ideal case even at small depths  $t$ . This offset reflects the intrinsic uncertainty induced by noise. Due to the computational cost of noisy simulation at larger scales, we turn to direct experiments on the IBM QPU ibm\_marrakesh for  $L = 20$  [71]. Constrained by available experimental resources, we use  $N_m = 4 \times 10^4$ ,  $N_e = 5 \times 10^3$  and  $M = 5$ . The resulting data, Fig. 4(c,d), show that  $\Delta$  increases with  $t$  and eventually saturates near  $2 \log(2)$ , demonstrating that the learnability transition persists on current noisy hardware. It is also noteworthy that  $\Delta$  at small  $t$  is lower than in the ibm\_brisbane simulations, consistent with the lower noise level of ibm\_marrakesh and the correspondingly reduced intrinsic uncertainty.

*Discussions*—Our results have several implications for extracting MIE in practice and for understanding fundamental limits of quantum learning. In the shallow-depth regime, the observed learnability indicates that

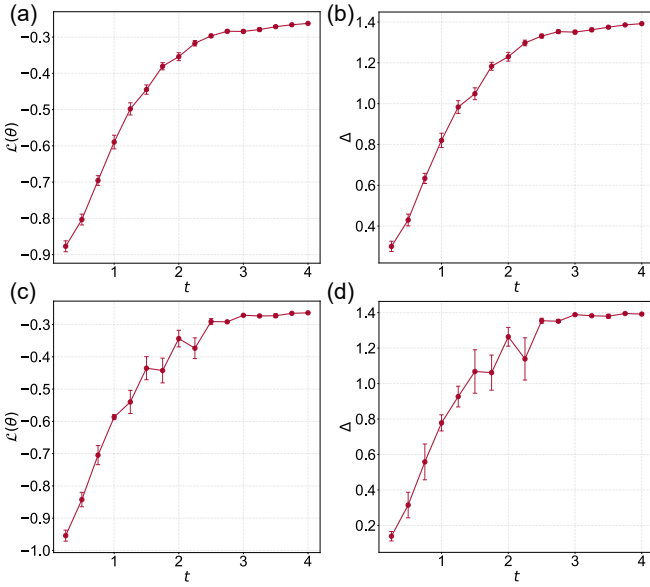


FIG. 4. Learnability transition in 1D all-to-all circuits with noise. (a,b)  $\mathcal{L}(\theta)$  and  $\Delta$  for  $L = 16$ , obtained from noisy classical simulations using the Qiskit noise snapshot of the IBM QPU `ibm_brisbane`. Here  $N_m = 2 \times 10^4$ ,  $N_p = 2 \times 10^4$ ,  $N_e = 5 \times 10^4$ , and  $M = 50$ . (c,d)  $\mathcal{L}(\theta)$  and  $\Delta$  for  $L = 20$ , obtained from experiments on the IBM QPU `ibm_marrakesh`. Here  $N_m = 4 \times 10^4$ ,  $N_p = 7 \times 10^4$ ,  $N_e = 5 \times 10^3$ , and  $M = 5$ .

neural networks trained solely on measurement data can serve as surrogates for classical simulation whenever the latter remains tractable. This demonstrates the possibility of deploying data-driven neural network decoders instead of simulation-based decoders for quantum error correction [72–76]. By contrast, the loss of learnability at large depth provides evidence for quantum advantage: when classical simulation becomes intractable, machine-learning approaches likewise fail to recover MIE with polynomial resources. This further suggests that in deep circuits within our setup, not only is substantial MIE generated, but crucially, this entanglement remains undetectable. Harnessing MIE in such regimes—rather than merely witnessing its presence—thus remains an important outstanding challenge.

Our work also suggests several interesting directions for future investigation. The present resource analysis accounts for quantum time complexity via  $N_m$  and classical space complexity through  $N_p$ , but does not incorporate the classical time complexity of training itself. Including training overhead would sharpen the boundary of efficient MIE extraction and is essential for a complete complexity-theoretic characterization. In addition, our study has focused on states generated by random circuits, which represent an average-case scenario. Since physically motivated states—e.g., ground states of interacting Hamiltonians or states with specific symmetries—typically exhibit structure absent in random en-

sembles, exploring learnability transitions in such settings is a natural and important next step. We leave this to future work.

*Acknowledgments*—We acknowledge Yi-Zhuang You and Pengfei Zhang for valuable discussions. This work is supported by the Natural Science Foundation of China through Grants No. 12350404 and No. 12174066, the Innovation Program for Quantum Science and Technology through Grant No. 2021ZD0302600, the Science and Technology Commission of Shanghai Municipality under Grants No. 23JC1400600, No. 24LZ1400100 and No. 2019SHZDZX01, and is sponsored by the “Shuguang Program” supported by the Shanghai Education Development Foundation and Shanghai Municipal Education Commission.

\* wjingphys@fudan.edu.cn

- [1] R. Horodecki, P. Horodecki, M. Horodecki, and K. Horodecki, Quantum entanglement, *Rev. Mod. Phys.* **81**, 865 (2009).
- [2] M. A. Nielsen and I. L. Chuang, *Quantum Computation and Quantum Information* (Cambridge University Press, Cambridge, 2010).
- [3] M. Wilde, *Quantum Information Theory*, 2nd ed. (Cambridge University Press, Cambridge, 2017).
- [4] C. L. Degen, F. Reinhard, and P. Cappellaro, Quantum sensing, *Rev. Mod. Phys.* **89**, 035002 (2017).
- [5] R. R. Allen, F. Machado, I. L. Chuang, H.-Y. Huang, and S. Choi, Quantum computing enhanced sensing, [arXiv:2501.07625](https://arxiv.org/abs/2501.07625) (2025).
- [6] C. H. Bennett, G. Brassard, C. Crépeau, R. Jozsa, A. Peres, and W. K. Wootters, Teleporting an unknown quantum state via dual classical and einstein-podolsky-rosen channels, *Phys. Rev. Lett.* **70**, 1895 (1993).
- [7] M. Popp, F. Verstraete, M. A. Martín-Delgado, and J. I. Cirac, Localizable entanglement, *Phys. Rev. A* **71**, 042306 (2005).
- [8] M. A. Rajabpour, Post-measurement bipartite entanglement entropy in conformal field theories, *Phys. Rev. B* **92**, 075108 (2015).
- [9] C.-J. Lin, W. Ye, Y. Zou, S. Sang, and T. H. Hsieh, Probing sign structure using measurement-induced entanglement, *Quantum* **7**, 910 (2023).
- [10] H. J. Briegel, D. E. Browne, W. Dür, R. Raussendorf, and M. Van den Nest, Measurement-based quantum computation, *Nat. Phys.* **5**, 19 (2009).
- [11] H. J. Briegel and R. Raussendorf, Persistent entanglement in arrays of interacting particles, *Phys. Rev. Lett.* **86**, 910 (2001).
- [12] L. Piroli, G. Styliaris, and J. I. Cirac, Quantum circuits assisted by local operations and classical communication: Transformations and phases of matter, *Phys. Rev. Lett.* **127**, 220503 (2021).
- [13] J. Y. Lee, W. Ji, Z. Bi, and M. Fisher, Decoding measurement-prepared quantum phases and transitions: From ising model to gauge theory, and beyond, [arXiv:2208.11699](https://arxiv.org/abs/2208.11699) (2022).
- [14] G.-Y. Zhu, N. Tantivasadakarn, A. Vishwanath,

S. Trebst, and R. Verresen, Nishimori's cat: Stable long-range entanglement from finite-depth unitaries and weak measurements, *Phys. Rev. Lett.* **131**, 200201 (2023).

[15] A. Cowsik, M. Ippoliti, and X.-L. Qi, Engineering entanglement geometry via spacetime-modulated measurements, *Phys. Rev. D* **112**, L081904 (2025).

[16] S.-K. Jian, C. Liu, X. Chen, B. Swingle, and P. Zhang, Measurement-induced phase transition in the monitored sachdev-ye-kitaev model, *Phys. Rev. Lett.* **127**, 140601 (2021).

[17] Z. Cheng, R. Wen, S. Gopalakrishnan, R. Vasseur, and A. C. Potter, Universal structure of measurement-induced information in many-body ground states, *Phys. Rev. B* **109**, 195128 (2024).

[18] M. Ippoliti, M. J. Gullans, S. Gopalakrishnan, D. A. Huse, and V. Khemani, Entanglement phase transitions in measurement-only dynamics, *Phys. Rev. X* **11**, 011030 (2021).

[19] A. Lavasani, Y. Alavirad, and M. Barkeshli, Measurement-induced topological entanglement transitions in symmetric random quantum circuits, *Nat. Phys.* **17**, 342 (2021).

[20] K. Klocke, D. Simm, G.-Y. Zhu, S. Trebst, and M. Buchhold, Entanglement dynamics in monitored kitaev circuits: Loop models, symmetry classification, and quantum lifshitz scaling, *Phys. Rev. B* **111**, 224301 (2025).

[21] Y. Li, X. Chen, and M. P. A. Fisher, Measurement-driven entanglement transition in hybrid quantum circuits, *Phys. Rev. B* **100**, 134306 (2019).

[22] B. Skinner, J. Ruhman, and A. Nahum, Measurement-induced phase transitions in the dynamics of entanglement, *Phys. Rev. X* **9**, 031009 (2019).

[23] M. Szyniszewski, A. Romito, and H. Schomerus, Entanglement transition from variable-strength weak measurements, *Phys. Rev. B* **100**, 064204 (2019).

[24] R. Vasseur, A. C. Potter, Y.-Z. You, and A. W. W. Ludwig, Entanglement transitions from holographic random tensor networks, *Phys. Rev. B* **100**, 134203 (2019).

[25] A. Nahum and B. Skinner, Entanglement and dynamics of diffusion-annihilation processes with majorana defects, *Phys. Rev. Research* **2**, 023288 (2020).

[26] A. Zabalo, M. J. Gullans, J. H. Wilson, S. Gopalakrishnan, D. A. Huse, and J. H. Pixley, Critical properties of the measurement-induced transition in random quantum circuits, *Phys. Rev. B* **101**, 060301 (2020).

[27] C.-M. Jian, Y.-Z. You, R. Vasseur, and A. W. W. Ludwig, Measurement-induced criticality in random quantum circuits, *Phys. Rev. B* **101**, 104302 (2020).

[28] Y. Bao, S. Choi, and E. Altman, Theory of the phase transition in random unitary circuits with measurements, *Phys. Rev. B* **101**, 104301 (2020).

[29] S. Choi, Y. Bao, X.-L. Qi, and E. Altman, Quantum Error Correction in Scrambling Dynamics and Measurement-Induced Phase Transition, *Phys. Rev. Lett.* **125**, 030505 (2020).

[30] X. Turkeshi, R. Fazio, and M. Dalmonte, Measurement-induced criticality in (2+1)-dimensional hybrid quantum circuits, *Phys. Rev. B* **102**, 014315 (2020).

[31] O. Alberton, M. Buchhold, and S. Diehl, Entanglement Transition in a Monitored Free-Fermion Chain: From Extended Criticality to Area Law, *Phys. Rev. Lett.* **126**, 170602 (2021).

[32] S. Sharma, X. Turkeshi, R. Fazio, and M. Dalmonte, Measurement-induced criticality in extended and long-range unitary circuits, *SciPost Phys. Core* **5**, 023 (2022).

[33] M. Block, Y. Bao, S. Choi, E. Altman, and N. Y. Yao, Measurement-induced transition in long-range interacting quantum circuits, *Phys. Rev. Lett.* **128**, 010604 (2022).

[34] P. Sierant, M. Schirò, M. Lewenstein, and X. Turkeshi, Measurement-induced phase transitions in  $(d + 1)$ -dimensional stabilizer circuits, *Phys. Rev. B* **106**, 214316 (2022).

[35] M. P. A. Fisher, V. Khemani, A. Nahum, and S. Vijay, Random Quantum Circuits, *Annu. Rev. Condens. Matter Phys.* **14**, 335 (2023).

[36] I. Pohoiko, I. V. Gornyi, and A. D. Mirlin, Measurement-induced phase transition for free fermions above one dimension, *Phys. Rev. Lett.* **132**, 110403 (2024).

[37] D. Qian and J. Wang, Protect measurement-induced phase transition from noise, *Phys. Rev. Lett.* **134**, 020403 (2025).

[38] J. M. Koh, S.-N. Sun, M. Motta, and A. J. Minnich, Measurement-induced entanglement phase transition on a superconducting quantum processor with mid-circuit readout, *Nat. Phys.* **19**, 1314 (2023).

[39] M. J. Gullans and D. A. Huse, Dynamical purification phase transition induced by quantum measurements, *Phys. Rev. X* **10**, 041020 (2020).

[40] M. J. Gullans and D. A. Huse, Scalable probes of measurement-induced criticality, *Phys. Rev. Lett.* **125**, 070606 (2020).

[41] C. Noel, P. Niroula, D. Zhu, A. Ringer, L. Egan, D. Biswas, M. Cetina, A. V. Gorshkov, M. J. Gullans, D. A. Huse, and C. Monroe, Measurement-induced quantum phases realized in a trapped-ion quantum computer, *Nat. Phys.* **18**, 760 (2022).

[42] H. Dehghani, A. Lavasani, M. Hafezi, and M. J. Gullans, Neural-network decoders for measurement induced phase transitions, *Nature Comm.* **14**, 2918 (2023).

[43] J. C. Hoke *et al.*, Measurement-induced entanglement and teleportation on a noisy quantum processor, *Nature* **622**, 481 (2023).

[44] U. Agrawal, J. Lopez-Piqueres, R. Vasseur, S. Gopalakrishnan, and A. C. Potter, Observing quantum measurement collapse as a learnability phase transition, *Phys. Rev. X* **14**, 041012 (2024).

[45] M. Ippoliti and V. Khemani, Learnability transitions in monitored quantum dynamics via eavesdropper's classical shadows, *PRX Quantum* **5**, 020304 (2024).

[46] Y. Li, Y. Zou, P. Glorioso, E. Altman, and M. P. A. Fisher, Cross entropy benchmark for measurement-induced phase transitions, *Phys. Rev. Lett.* **130**, 220404 (2023).

[47] H. Kamakari, J. Sun, Y. Li, J. J. Thio, T. P. Gujarati, M. P. A. Fisher, M. Motta, and A. J. Minnich, Experimental demonstration of scalable cross-entropy benchmarking to detect measurement-induced phase transitions on a superconducting quantum processor, *Phys. Rev. Lett.* **134**, 120401 (2025).

[48] D. Qian and J. Wang, Coherent information phase transition in a noisy quantum circuit, *Phys. Rev. B* **112**, L180301 (2025).

[49] X. Turkeshi, Measurement-induced criticality as a data-structure transition, *Phys. Rev. B* **106**, 144313 (2022).

[50] D. Qian and J. Wang, Steering-induced phase transition in measurement-only quantum circuits, *Phys. Rev. B* **109**, 024301 (2024).

[51] H. Kim, A. Kumar, Y. Zhou, Y. Xu, R. Vasseur, and E.-A. Kim, Learning measurement-induced phase transitions using attention, [arXiv:2508.15895](https://arxiv.org/abs/2508.15895) (2025).

[52] S. J. Garratt and E. Altman, Probing postmeasurement entanglement without postselection, *PRX Quantum* **5**, 030311 (2024).

[53] M. McGinley, Postselection-free learning of measurement-induced quantum dynamics, *PRX Quantum* **5**, 020347 (2024).

[54] H.-Y. Huang, R. Kueng, and J. Preskill, Information-theoretic bounds on quantum advantage in machine learning, *Phys. Rev. Lett.* **126**, 190505 (2021).

[55] H.-Y. Huang, R. Kueng, G. Torlai, V. V. Albert, and J. Preskill, Provably efficient machine learning for quantum many-body problems, *Science* **377**, eabk3333 (2022).

[56] Y. Du, Y. Zhu, Y.-H. Zhang, M.-H. Hsieh, P. Rebentrost, W. Gao, Y.-D. Wu, J. Eisert, G. Chiribella, D. Tao, *et al.*, Artificial intelligence for representing and characterizing quantum systems, [arXiv:2509.04923](https://arxiv.org/abs/2509.04923) (2025).

[57] W. Hou, S. J. Garratt, N. M. Eassa, E. Rosenberg, P. Roushan, Y.-Z. You, and E. Altman, Machine learning the effects of many quantum measurements, [arXiv:2509.08890](https://arxiv.org/abs/2509.08890) (2025).

[58] H.-Y. Huang, R. Kueng, and J. Preskill, Predicting many properties of a quantum system from very few measurements, *Nat. Phys.* **16**, 1050 (2020).

[59] See Supplemental Material for more details.

[60] A. Vaswani, N. Shazeer, N. Parmar, J. Uszkoreit, L. Jones, A. N. Gomez, L. Kaiser, and I. Polosukhin, Attention is all you need, in *Proceedings of the 31st International Conference on Neural Information Processing Systems*, Vol. 30 (2017) pp. 6000–6010.

[61] J. Devlin, M.-W. Chang, K. Lee, and K. Toutanova, Bert: Pre-training of deep bidirectional transformers for language understanding, in *Proceedings of the 2019 conference of the North American chapter of the association for computational linguistics: human language technologies, volume 1 (long and short papers)* (2019) pp. 4171–4186.

[62] Y. Bao, M. Block, and E. Altman, Finite-Time Teleportation Phase Transition in Random Quantum Circuits, *Phys. Rev. Lett.* **132**, 030401 (2024).

[63] J. C. Napp, R. L. La Placa, A. M. Dalzell, F. G. S. L. Brandão, and A. W. Harrow, Efficient classical simulation of random shallow 2d quantum circuits, *Phys. Rev. X* **12**, 021021 (2022).

[64] M. Yoganathan, A condition under which classical simulability implies efficient state learnability, [arXiv:1907.08163](https://arxiv.org/abs/1907.08163) (2019).

[65] L. G. Valiant, A theory of the learnable, *Commun. ACM* **27**, 1134–1142 (1984).

[66] F. Arute, K. Arya, R. Babbush, D. Bacon, J. C. Bardin, R. Barends, R. Biswas, S. Boixo, F. G. Brandao, D. A. Buell, *et al.*, Quantum supremacy using a programmable superconducting processor, *Nature* **574**, 505 (2019).

[67] S.-B. B. Lee, H. R. Choi, D. D. Ohm, and S.-S. B. Lee, Scalable projected entangled-pair state representation of random quantum circuit states, *Phys. Rev. Res.* **7**, 033252 (2025).

[68] A. Bene Watts, D. Gosset, Y. Liu, and M. Soleimanifar, Quantum advantage from measurement-induced entanglement in random shallow circuits, *PRX Quantum* **6**, 010356 (2025).

[69] M. McGinley, W. W. Ho, and D. Malz, Measurement-induced entanglement and complexity in random constant-depth 2d quantum circuits, *Phys. Rev. X* **15**, 021059 (2025).

[70] C. Cao and J. Eisert, Measurement-driven quantum advantages in shallow circuits, [arXiv:2505.04705](https://arxiv.org/abs/2505.04705) (2025).

[71] M. AbuGhanem, Ibm quantum computers: evolution, performance, and future directions, *J. Supercomput.* **81**, 687 (2025).

[72] G. Torlai and R. G. Melko, Neural decoder for topological codes, *Phys. Rev. Lett.* **119**, 030501 (2017).

[73] J. Bausch, A. W. Senior, F. J. Heras, T. Edlich, A. Davies, M. Newman, C. Jones, K. Satzinger, M. Y. Niu, S. Blackwell, *et al.*, Learning high-accuracy error decoding for quantum processors, *Nature* **635**, 834 (2024).

[74] B. M. Varbanov, M. Serra-Peralta, D. Byfield, and B. M. Terhal, Neural network decoder for near-term surface-code experiments, *Phys. Rev. Res.* **7**, 013029 (2025).

[75] G. Hu, W. Ouyang, C.-Y. Lu, C. Lin, and H.-S. Zhong, Efficient and universal neural-network decoder for stabilizer-based quantum error correction, [arXiv:2502.19971](https://arxiv.org/abs/2502.19971) (2025).

[76] Y. Zhou, C. Wan, Y. Xu, J. P. Zhou, K. Q. Weinberger, and E.-A. Kim, Learning to decode logical circuits, *Nat. Comput. Sci.* (2025).

# Supplemental Material for “Data-Driven Learnability Transition of Measurement-Induced Entanglement”

Dongheng Qian<sup>1, 2</sup> and Jing Wang<sup>1, 2, 3, 4, \*</sup>

<sup>1</sup>*State Key Laboratory of Surface Physics and Department of Physics, Fudan University, Shanghai 200433, China*

<sup>2</sup>*Shanghai Research Center for Quantum Sciences, Shanghai 201315, China*

<sup>3</sup>*Institute for Nanoelectronic Devices and Quantum Computing, Fudan University, Shanghai 200433, China*

<sup>4</sup>*Hefei National Laboratory, Hefei 230088, China*

## CONTENTS

S1. Model Architecture	1
S2. Training Detail	2
S3. Alternative Loss Function	2
S4. More Numerical Results	5
References	6

## S1. MODEL ARCHITECTURE

We employ an end-to-end learning framework based on a transformer encoder to map binary measurement sequences  $\{+1, -1\}$  to a  $4 \times 4$  complex-valued density matrices that satisfy quantum mechanical constraints. The architecture consists of two main components: a BERT encoder that processes the input sequence and extracts the [CLS] token representation [1], and a specialized density matrix generation head that produces the final output.

Our encoder follows the standard transformer architecture with a vocabulary size of 3 [2], corresponding to the classification token and the two types of measurement outcomes. The input to the model is a binary measurement sequence, with a special [CLS] token prepended at the beginning. The input processing proceeds as follows: each token in the sequence is mapped through a trainable embedding layer to a  $d_h$ -dimensional vector, where  $d_h$  denotes the hidden dimension of the model. Simultaneously, each position in the sequence is encoded by a learnable positional embedding, also of dimension  $d_h$ . Unlike the original transformer which uses fixed sinusoidal position encodings, we employ learnable positional embeddings that are jointly optimized during training, allowing the model to adapt its positional representations to the specific structure of quantum measurement sequences [1]. For the two-dimensional case, we use the same approach, as we expect the positional embeddings to capture the underlying two-dimensional structure of the measurement sequence. The token embeddings and positional embeddings are then element-wise added to form the input representation.

This input representation is processed by  $N_l$  stacked transformer encoder layers. Each layer consists of two sub-components connected by residual connections: a multi-head self-attention mechanism and a position-wise feed-forward network. We adopt the Pre-LN architecture where layer normalization is applied before each sub-component rather than after [3]. In the multi-head self-attention mechanism, the input of dimension  $d_h$  is linearly projected into queries, keys, and values for  $N_h$  parallel attention heads, each operating on a subspace of dimension  $d = d_h/N_h$ . The scaled dot-product attention is computed independently for each head as  $\text{Attention}(Q, K, V) = \text{softmax}(QK^T/\sqrt{d})V$ . The outputs from all heads are concatenated and linearly projected back to dimension  $d_h$ , followed by dropout and residual connection with the input. Throughout the work, we choose  $N_h = 4$ . The output of the attention sub-layer is then fed into the position-wise feed-forward network, which consists of two linear transformations with a ReLU activation in between. The first linear layer expands the representation from dimension  $d_h$  to an intermediate dimension  $d_f$ , applies ReLU activation, and the second linear layer projects it back to dimension  $d_h$ . This is again followed by dropout and a residual connection. Dropout with a rate of 0.1 is applied before each residual connection,

---

\* [wjingphys@fudan.edu.cn](mailto:wjingphys@fudan.edu.cn)

and an independent attention dropout with rate 0.1 is applied to the attention weights. After passing through all  $N_l$  encoder layers, we extract the final hidden state corresponding to the [CLS] token position, which serves as a fixed-dimensional representation of the entire input sequence. This [CLS] representation, a vector of dimension  $d_h$ , is then fed into the density matrix generation head.

The density matrix head maps the [CLS] token representation from the BERT encoder to a complex-valued density matrix through an  $AA^\dagger$  decomposition that automatically satisfies all quantum mechanical constraints. Initially, a linear projection maps the [CLS] representation to 32 real-valued parameters, which are then reshaped into a complex matrix  $A \in \mathbb{C}^{4 \times 4}$  by interpreting consecutive pairs of parameters as the real and imaginary components. The unnormalized density matrix is computed as  $\rho_0 = AA^\dagger$ , which is then trace-normalized to satisfy  $\rho_{\text{norm}} = \rho_0 / \text{Tr}(\rho_0)$ . Finally, we apply  $\varepsilon$ -mixing through a convex combination  $\rho = (1 - \varepsilon)\rho_{\text{norm}} + \varepsilon I$ , where  $\varepsilon = 0.0001$  is a small mixing parameter and  $I$  is the identity matrix. The  $\varepsilon$ -mixing step here prevents numerical instabilities associated with near-zero eigenvalues during training. This construction method ensures that all physical constraints required of quantum density matrices are rigorously satisfied. Hermiticity ( $\rho = \rho^\dagger$ ) is automatically satisfied by the  $AA^\dagger$  construction since  $(AA^\dagger)^\dagger = (A^\dagger)^\dagger A^\dagger = AA^\dagger$ . Positive semi-definiteness with all eigenvalues bounded below by  $\varepsilon$  is explicitly ensured through the  $\varepsilon$ -mixing step, which expresses the output as a convex combination of the learned density matrix and the maximally mixed state. The unit trace constraint  $\text{Tr}(\rho) = 1$  is enforced through explicit trace normalization.

The majority of trainable parameters reside in the transformer encoder. To construct models with varying parameter numbers, we adjust three key architectural hyperparameters: the hidden dimension  $d_h$ , the feed-forward intermediate dimension  $d_f$ , and the number of encoder layers  $N_l$ . We constructed four models with different number of parameters, and the relationship between model size and architectural configuration is summarized in Table I.

Model Parameters	$d_h$	$d_f$	$N_l$
20K	32	64	2
70K	64	128	2
270K	128	256	2
540K	128	256	4

TABLE I. Model configurations for different parameter numbers.

## S2. TRAINING DETAIL

We optimize the model using the AdamW optimizer with an initial learning rate of  $\eta_0 = 5 \times 10^{-4}$  and weight decay of 0.01, which implements  $L_2$ -regularization through a decoupled weight decay parameter separate from the gradient-based updates. The learning rate follows a cosine annealing schedule with warmup: during an initial warmup phase comprising 10% of total training steps, the learning rate increases linearly from zero to  $\eta_0$ , after which it gradually decreases following a cosine curve to a minimum value of  $\eta_{\text{min}} = 10^{-5}$  to improve convergence to sharp minima. We apply global gradient norm clipping with a threshold of 1.0 to prevent gradient explosion, particularly important when training with complex-valued operations. Weight decay regularization is applied to all parameters except biases and layer normalization parameters, following standard practice in transformer training. The entire model is implemented in pure PyTorch, with no reliance on pre-trained weights; all components are trained from scratch. All the training is conducted on one 24GB NVIDIA 4090 GPU, one 48GB Ada6000 GPU and one 80GB A100 GPU. For all the cases, the batch size is set to match the total number of data. Throughout the study, we set the number of epochs to 500, and typical training loss evolution over the epochs is shown in Fig. S1.

## S3. ALTERNATIVE LOSS FUNCTION

Besides the loss function we introduced in the main text, there are other possible choices of loss functions. For example, consider the inequality:

$$\mathbb{E}_m \mathbb{E}_s [\text{Tr}(\rho_{AB,m} \sigma_{AB,m}^s)] = \mathbb{E}_m [\text{Tr}(\rho_{AB,m} \sigma_{AB,m})] \leq 1, \quad (\text{S1})$$

where equality holds if and only if  $\rho_{AB,m} = \sigma_{AB,m}$  for every  $m$ , assuming  $\sigma_{AB,m}$  is pure. This motivates the following alternative loss function:

$$\mathcal{L}_1(\theta) = -\mathbb{E}_m \mathbb{E}_s [\text{Tr}(\rho_{AB,m} \sigma_{AB,m}^s)]. \quad (\text{S2})$$

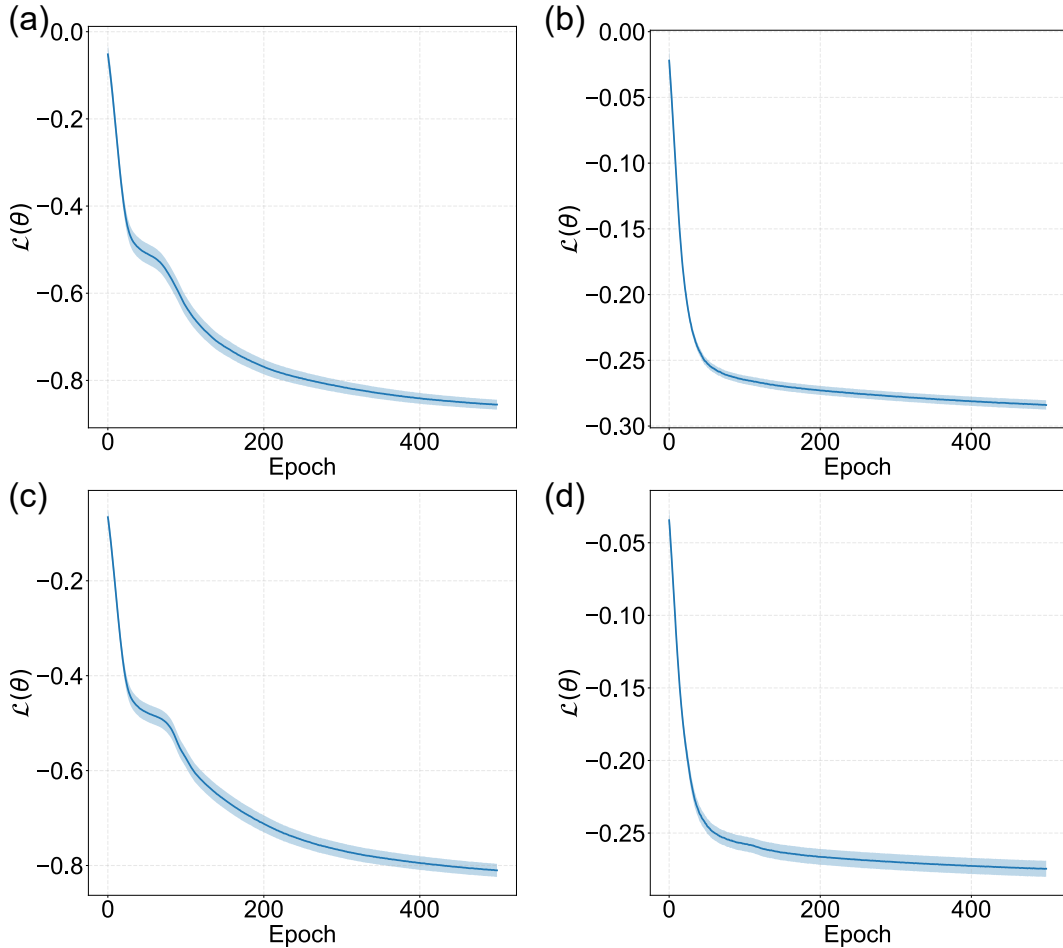


FIG. S1.  $\mathcal{L}(\theta)$  evolution during the training process. Here,  $N_m = 8 \times 10^4$  and  $N_p = 7 \times 10^4$ . The shaded area represents the standard error over  $M = 50$  circuit realizations. (a-b) Training for one-dimensional all-to-all circuits with  $L = 20$ , at  $t = 1$  and  $t = 3.5$ , respectively. (c-d) Training for two-dimensional nearest neighbor circuits with  $L = 5 \times 5$ , at  $t = 1.6$  and  $t = 6.4$ , respectively.

Note that this loss function is applicable only when the pre-measurement state is pure. There are two key differences between  $\mathcal{L}_1(\theta)$  and the loss function presented in the main text. First, accurate estimation of  $\mathcal{L}_1(\theta)$  requires fewer samples than  $\mathcal{L}(\theta)$ , as the variance arises primarily from the term  $\text{Tr}(\rho_{AB,m} \sigma_{AB,m}^s)$ , which leads to  $\mathcal{L}_1(\theta)$  having a variance approximately four times smaller than that of  $\mathcal{L}(\theta)$ . Second,  $\mathcal{L}_1(\theta)$  inherently encourages the model to output pure states, whereas  $\mathcal{L}(\theta)$  does not exhibit such a preference. In the case of  $\mathcal{L}_1(\theta)$ , the term  $\text{Tr}(\rho_{AB,m} \sigma_{AB,m}^s)$  maximizes the overlap between  $\rho_{AB,m}$  and  $\sigma_{AB,m}^s$ , which is a linear functional over the convex set of density matrices. Since the extremum of a linear functional on a convex set always lies at the boundary, the optimal solution is a pure state, corresponding to the eigenvector of  $\sigma_{AB,m}^s$  with the largest eigenvalue. In contrast, the extra quadratic term in  $\mathcal{L}(\theta)$  penalizes the purity of the output state, thereby promoting mixed-state estimations. To further demonstrate this distinction, we compare models trained under these two loss functions by calculating the average entanglement entropy of the output state  $\rho_{AB,m}$ . As shown in Fig. S2, the entanglement entropy for the model trained with  $\mathcal{L}_1(\theta)$  remains small across all  $t$ , whereas for the model trained with  $\mathcal{L}(\theta)$ , the state  $\rho_{AB,m}$  approaches the maximally mixed state at large  $t$ , as evidenced by its near-maximal entanglement entropy.

Despite these differences, the learnability transition persists when  $\mathcal{L}_1(\theta)$  is used as the loss function. As is shown in Fig. S3, for small  $t$ , increasing either the amount of measurement data or the number of model parameters reduces the uncertainty  $\Delta$ , consistent with the learnable phase. By contrast, at large  $t$ ,  $\Delta$  saturates and grows as resources are further increased, indicating an unlearnable phase. A notable distinction from using  $\mathcal{L}(\theta)$  is that, in this case,  $\Delta$  can grow well beyond  $2 \log(2)$ . This occurs because, although the model outputs nearly pure states even at large  $t$ , the learned state  $\rho_{AB,m}$  becomes nearly orthogonal to the true state  $\sigma_{AB,m}$ , yielding large  $\Delta$ .

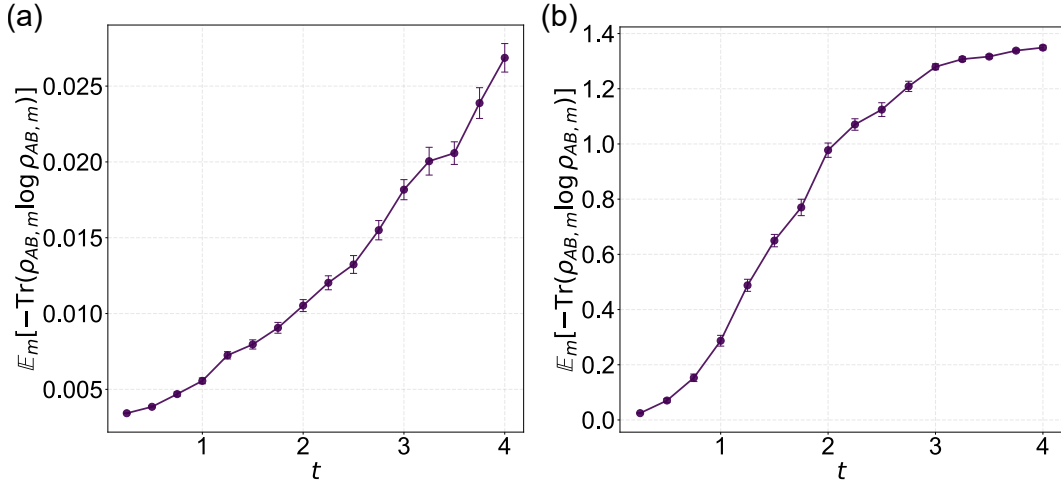


FIG. S2. Comparison of loss functions for random one-dimensional all-to-all circuits with  $L = 20$ ,  $N_m = 8 \times 10^4$ ,  $N_p = 7 \times 10^4$ , and  $N_e = 5 \times 10^4$ . Error bars represent the standard error over  $M = 50$  circuit realizations. (a) Model trained with  $\mathcal{L}_1(\theta)$ . (b) Model trained with  $\mathcal{L}(\theta)$ .

Another related loss function can be constructed as follows. Consider the raw shadow state on  $AB$  given by:

$$\tilde{\sigma}_{AB,m}^s = ((U_A^s)^{-1} |m_A\rangle \langle m_A| U_A^s) \otimes ((U_B^s)^{-1} |m_B\rangle \langle m_B| U_B^s). \quad (\text{S3})$$

The loss function  $\mathcal{L}_2(\theta) = -\mathbb{E}_m \mathbb{E}_s \text{Tr}(\rho_{AB,m} \tilde{\sigma}_{AB,m}^s)$  was previously considered in [4]. However, we demonstrate that this loss function is valid only when the post-measurement state  $\sigma_{AB,m}$  possesses a flat entanglement spectrum. Recall that the shadow snapshot is given by:

$$\sigma_{AB,m}^s = (3(U_A^s)^{-1} |m_A\rangle \langle m_A| U_A^s - I) \otimes (3(U_B^s)^{-1} |m_B\rangle \langle m_B| U_B^s - I), \quad (\text{S4})$$

where  $I$  denotes the  $2 \times 2$  identity matrix. Since  $\mathbb{E}_s[\sigma_{AB,m}^s] = \sigma_{AB,m}$ , we have:

$$\mathbb{E}_s[\tilde{\sigma}_{AB,m}^s] = \frac{1}{9}(\sigma_{AB,m} + \sigma_{A,m} \otimes I + I \otimes \sigma_{B,m} + I \otimes I). \quad (\text{S5})$$

Consequently, the loss function simplifies to:

$$\mathcal{L}_2(\theta) = -\frac{1}{9} \mathbb{E}_m \text{Tr}(\rho_{AB,m} \Omega), \quad (\text{S6})$$

where we define the effective operator  $\Omega \equiv \sigma_{AB,m} + \sigma_{A,m} \otimes I + I \otimes \sigma_{B,m} + I \otimes I$ . We now show that for each measurement outcome  $m$ , the maximizer  $\text{argmax}_{\rho_{AB,m}} \text{Tr}(\rho_{AB,m} \Omega)$  coincides with the true state  $\sigma_{AB,m}$  if and only if  $\sigma_{AB,m}$  has a flat entanglement spectrum. Let  $\sigma_{AB,m} = |\psi\rangle \langle \psi|$ . Utilizing the Schmidt decomposition, we can write  $|\psi\rangle = \sum_k \sqrt{\lambda_k} |k\rangle_A \otimes |k\rangle_B$ . The reduced density matrices are:

$$\sigma_{A,m} = \sum_k \lambda_k |k\rangle_A \langle k|_A, \quad \sigma_{B,m} = \sum_k \lambda_k |k\rangle_B \langle k|_B. \quad (\text{S7})$$

For  $\text{argmax}_{\rho_{AB,m}} \text{Tr}(\rho_{AB,m} \Omega) = \sigma_{AB,m}$  to hold, the state  $|\psi\rangle$  must be an eigenvector of  $\Omega$ , i.e.,  $\Omega |\psi\rangle \propto |\psi\rangle$ . Applying  $\Omega$  to the state  $|\psi\rangle$  yields:

$$\Omega |\psi\rangle = \sum_k \sqrt{\lambda_k} (2 + 2\lambda_k) |k\rangle_A |k\rangle_B. \quad (\text{S8})$$

Therefore, the eigenvector condition requires the coefficient  $2 + 2\lambda_k$  to be independent of  $k$ , which implies that all non-zero Schmidt coefficients  $\lambda_k$  must be equal. Therefore, if the true post-measurement state  $\sigma_{AB,m}$  has a nontrivial entanglement spectrum—as is typical in our setup—this loss function fails to correctly train the model.

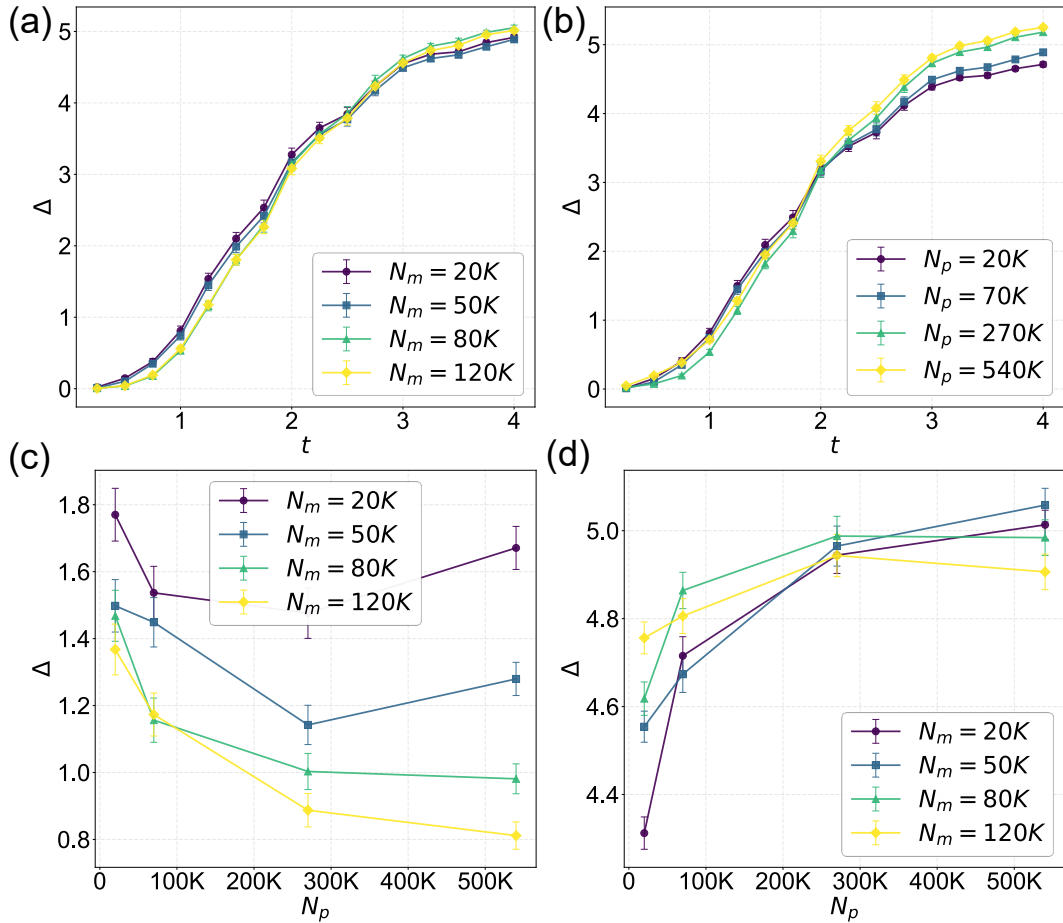


FIG. S3. Learnability transition in one-dimensional all-to-all circuits with  $\mathcal{L}_1(\theta)$  as the loss function. Here  $L = 20$ ,  $N_e = 5 \times 10^4$  and  $M = 50$ . (a)  $\Delta$  as a function of  $t$  for different  $N_m$ , with  $N_p = 7 \times 10^4$  fixed. (b)  $\Delta$  as a function of  $t$  for different  $N_p$ , with  $N_m = 5 \times 10^4$  fixed. (c,d)  $\Delta$  as a function of  $N_m$  and  $N_p$  for  $t = 1.25$  and  $t = 3.5$ , respectively.

#### S4. MORE NUMERICAL RESULTS

In this section, we present additional numerical results that support the learnability transition. In Fig. S4 and Fig. S5, we show  $\Delta$  for a range of combinations of  $N_m$  and  $N_p$  across all circuit depth  $t$ , for the one-dimensional all-to-all circuits and the two-dimensional nearest-neighbor circuits, respectively. A clear trend is that as  $N_m$  increases,

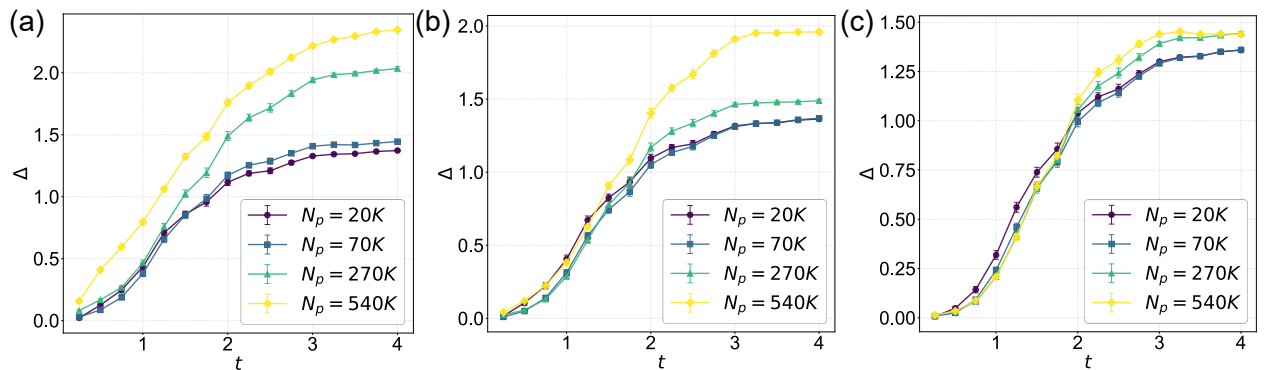


FIG. S4. Learnability transition in one-dimensional all-to-all circuits.  $\Delta$  as a function of  $t$  for different  $N_p$ , with different  $N_m$  being fixed. Here  $L = 20$ ,  $N_e = 5 \times 10^4$  and  $M = 50$ . (a)  $N_m = 2 \times 10^4$ . (b)  $N_m = 5 \times 10^4$ . (c)  $N_m = 1.2 \times 10^5$ .

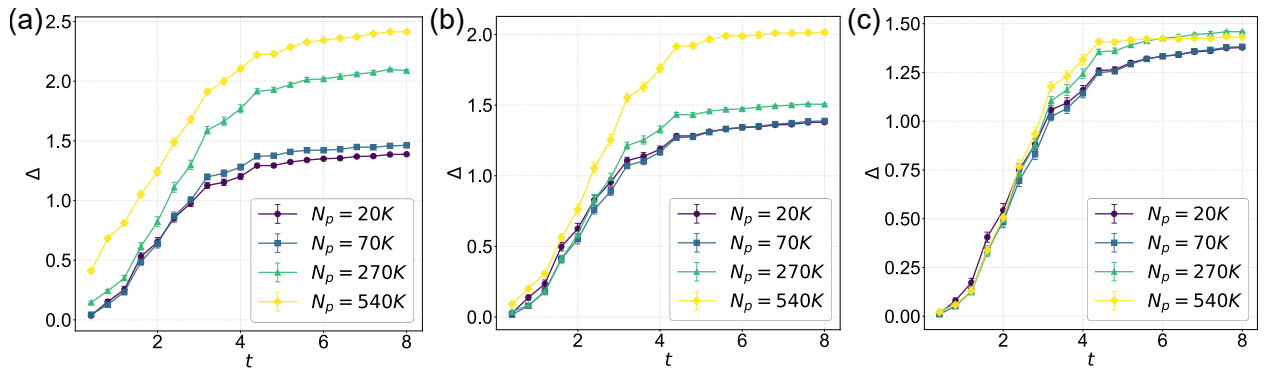


FIG. S5. Learnability transition in two-dimensional nearest-neighbor circuit circuits.  $\Delta$  as a function of  $t$  for different  $N_p$ , with different  $N_m$  being fixed. Here  $L = 5 \times 5$ ,  $N_e = 5 \times 10^4$  and  $M = 50$ . (a)  $N_m = 2 \times 10^4$ . (b)  $N_m = 5 \times 10^4$ . (c)  $N_m = 1.2 \times 10^5$ .

overfitting effects are mitigated, and a pronounced crossing becomes visible—below the crossing, larger  $N_p$  reduces  $\Delta$ ; whereas above it, increasing  $N_p$  leads to larger  $\Delta$ . This behavior is consistent with the presence of two distinct phases, corresponding to the learnable and unlearnable regimes.

---

[1] J. Devlin, M.-W. Chang, K. Lee, and K. Toutanova, Bert: Pre-training of deep bidirectional transformers for language understanding, in *Proceedings of the 2019 conference of the North American chapter of the association for computational linguistics: human language technologies, volume 1 (long and short papers)* (2019) pp. 4171–4186.

[2] A. Vaswani, N. Shazeer, N. Parmar, J. Uszkoreit, L. Jones, A. N. Gomez, L. Kaiser, and I. Polosukhin, Attention is all you need, in *Proceedings of the 31st International Conference on Neural Information Processing Systems*, Vol. 30 (2017) pp. 6000–6010.

[3] A. Radford, J. Wu, R. Child, D. Luan, D. Amodei, I. Sutskever, *et al.*, Language models are unsupervised multitask learners, *OpenAI blog* **1**, 9 (2019).

[4] W. Hou, S. J. Garratt, N. M. Eassa, E. Rosenberg, P. Roushan, Y.-Z. You, and E. Altman, Machine learning the effects of many quantum measurements, [arXiv:2509.08890](https://arxiv.org/abs/2509.08890) (2025).